Chapter 2
The LHC and the ATLAS Experiment

The big giant in current particle physics, the Large Hadron Collider (LHC) at CERN is the collider operated at the highest center-of-mass energy in the world. The ATLAS detector at the LHC is an apparatus to open up unknown physics at the energy frontier. In this chapter, technical details of the LHC and the ATLAS detector are described.

2.1 The Large Hadron Collider

The LHC [1] is a double-ring collider constructed at about 100 m underground at CERN and its neighborhood. The long circumference of 26.7 km and the strong magnetic field of 8.33 T produced by the superconductive dipole magnets achieve high center-of-mass energy proton-proton (pp) collisions at $\sqrt{s} = 14$ TeV at the designed value. Proton (or heavy ion) bunches are injected from the booster accelerator, the Super Proton Synchrotron (SPS). The bunches are accelerated in opposite directions in each ring, and collided at four bunch crossing points for the ATLAS, CMS, LHCb and ALICE experiments as shown in Fig. 2.1. The ATLAS and CMS are multi-purpose experiments which require high rate of pp collisions to study rare physics signatures; the LHCb detector is designed to study B-physics; and the ALICE is dedicated to study heavy ion collisions.

The expected number of events in pp collisions for a given period is described as

$$N_{\text{events}} = \sigma_{\text{process}} \int \mathcal{L} dt, \tag{2.1}$$

where σ_{process} is the cross section of the target physics process and $\mathcal{L}$ is an instantaneous luminosity. Assuming Gaussian beam distribution, the luminosity can be determined by beam parameters as:

T. Nobe, *Search for Scalar Top Quarks and Higgsino-Like Neutralinos*,
Springer Theses, DOI 10.1007/978-981-10-0003-4_2

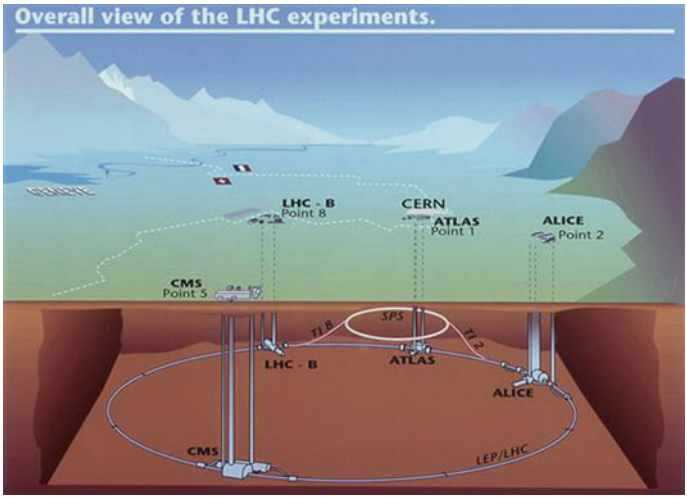

Fig. 2.1 The overall view of the LHC experiment [2]. The proton beam is injected from the SPS and accelerated up-to 7 TeV (designed value). Heavy ion beam can also be accelerated. There are four points of bunch crossing, where the ATLAS, CMS, LHCb and ALICE experiments are located

$$\mathcal{L} = \frac{N_b^2 n_b f_{\text{rev}} \gamma_r}{4\pi \epsilon_n \beta^*} F, \tag{2.2}$$

where N_b is the number of particles per bunch, n_b the number of bunches per beam, f_{rev} the revolution frequency, γ_r the relativistic gamma factor, ϵ_n the normalized transverse beam emittance,[1] β^* the beta function at the collision point,[2] and F the geometric luminosity reduction factor due to the crossing angle at the interaction point given by:

$$F = \left(1 + \left(\frac{\theta_c \sigma_z}{2\sigma^*}\right)^2\right)^{-1}, \tag{2.3}$$

where θ_c is the full crossing angle at the interaction point and σ_z the RMS bunch length. The above expression assumes round beams, with $\sigma_z \ll \beta^*$, and with equal beam parameters for both beams. Thus, the $\mathcal{L}$ indicates the power of the collider. The designed instantaneous luminosity for the ATLAS and CMS experiments is $\mathcal{L} = 10^{34}\,\text{cm}^{-2}\text{s}^{-1}$.

During the period between 2009 and 2012, referred as the LHC Run1, the LHC was operated at $\sqrt{s} = 7$–8 TeV and the maximum instantaneous luminosity observed

[1] The normalized transverse beam emittance ϵ_n is the average of the beam spread normalized in transverse direction [3].

[2] The β^* is a parameter of how much the beam is squeezed at the interaction point i.e. the transverse RMS beam size at the interaction point $\sigma^* = \sqrt{\epsilon_n \beta^*}/\gamma_r$ [3].

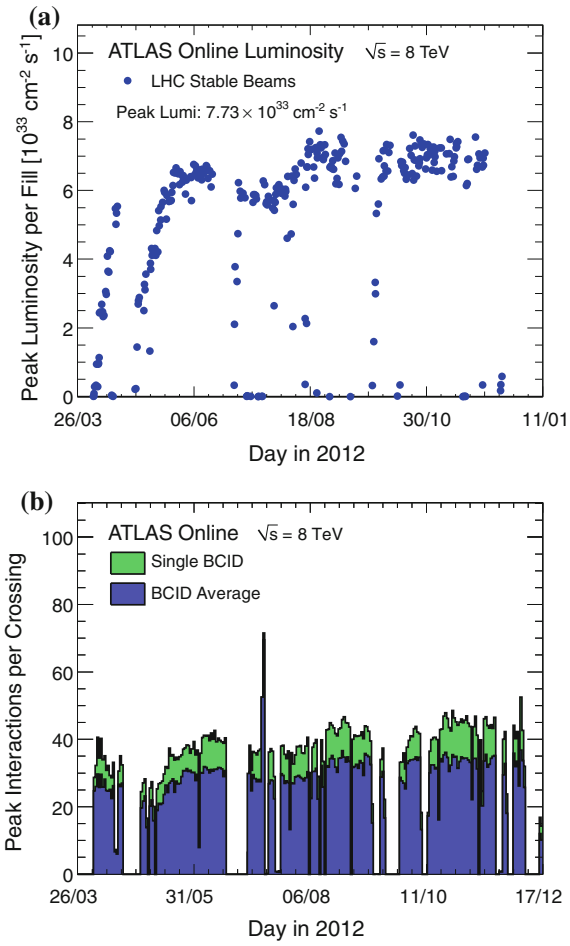

Fig. 2.2 **a** The maximum instantaneous luminosity versus day delivered to ATLAS [4]. Only the peak luminosity during stable beam periods is shown. **b** The maximum mean number of events per beam crossing (pileup) as a function of day in 2012, determined for each bunch [4]. The maximum pileup for any bunch is shown in *green*, as well as the maximum pileup averaged over all the colliding bunches shown in *blue*

with the ATLAS detector[3] was $\mathcal{L} = 7.7 \times 10^{33}\,\mathrm{cm}^{-2}\mathrm{s}^{-1}$. Figure 2.2a shows the peak luminosity recorded with the ATLAS detector as a function of day in year 2012. Multiple interactions, what we call 'pileup', take place during one bunch crossing due to high luminosity and short bunch crossing space (50 ns in 2012). The averaged number of interactions per bunch crossing was $\langle\mu\rangle \simeq 35$ in 2012, as shown in Fig. 2.2b. It is challenging to reconstruct target physics while avoiding the effect of the pileup.

The LHC is shut down between 2013 and 2015 for the upgrade of the facilities to perform the higher center-of-mass energy and luminosity. The LHC Run2 will start from 2015, in which we expect $\sqrt{s} = 13$ TeV and $\mathcal{L} = 1.6\text{–}2.3 \times 10^{34}\,\mathrm{cm}^{-2}\mathrm{s}^{-1}$.

[3]The criteria to measure the $\mathcal{L}$ and $\langle\mu\rangle$ is explained in Sect. 3.1.2.

Table 2.1 Important parameters of the LHC recorded in 2012 (Run1) [3, 5] with the ATLAS detector in comparison with the expected values in 2015 (Run2) [5] and the designed values [1]

Parameter	Run1 recorded	Run2 expected	Designed
E_{CM} (TeV)	8	13	14
N_b (10^{11})	1.7	1.15–1.6	1.15
$n_b^{\max}$	1374	1260–2760	2808
ϵ_n (μm)	2.5	1.6–3.75	3.75
β^* (cm)	60	60–70	55
θ_c (μrad)	290	230–380	285
$\mathcal{L}$ (10^{34} cm^{-2}s^{-1})	0.77	1.6–2.3	1.0
Bunch space (ns)	50	25–50	25
$\langle\mu\rangle$	∼35	up-to ∼100	∼23

E_{CM} is the center-of-mass energy, N_b the number of particles per bunch, n_b^{max} the maximum number of bunches in each proton beam, ϵ_n the normalized transverse beam emittance, θ_c the full crossing angle, β^* the beta function, $\mathcal{L}$ the instantaneous luminosity, and $\langle\mu\rangle$ the averaged number of interactions per bunch crossing (number of pileup)

Much higher luminosity than the designed value is scheduled, which leads to very high pileup environment (over 100 if the bunch spacing is 50 ns).

Recorded parameters in 2012 are summarized in Table 2.1 compared with the expected values in the LHC Run2 and the designed values.

2.2 The ATLAS Detector

ATLAS (A Troidal LHC ApparatuS) [6] is one of the pp colliding experiments at the LHC. Figure 2.3 illustrates the overall view of the ATLAS detector. The ATLAS detector is a multi-purpose apparatus whose height, length and weight are 25 m, 44 m, and 7,000 t, respectively. The detector consists of, from inside to outside, the inner detectors, electromagnetic and hadronic calorimeters, and muon spectrometers. The coverage of the detector is approximately 4π of the solid angle to detect secondary particles produced in pp collisions as much as possible to reconstruct the kinematics at the interaction point.

The ATLAS detector is forward-backward asymmetric with respect to the interaction point. We take cylindrical coordinate system of (r, z, ϕ), where z-axis is defined along beam pipe direction and the origin at the interaction point in the center of the detector, r-coordinate is orthogonal to that and ϕ is an azimuthal angle.[4] The rapidity y is defined as:

[4] ATLAS uses a right-handed coordinate system: x-axis points to the ring center, y-axis points upward, and $\phi = 0$ is along x-axis so that the upper half of the detector is described by $0 < \phi < \pi$ and the lower half by $\pi < \phi < 2\pi$.

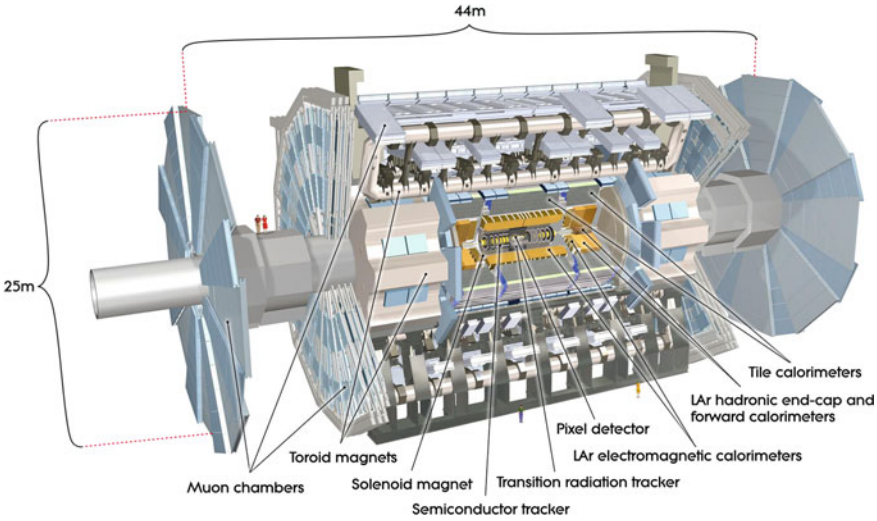

Fig. 2.3 The overall view of the ATLAS detector [6]. It consists of the inner detectors (pixel detector, semiconductor tracker, and transition radiation tracker), electromagnetic and hadronic calorimeters, and muon chambers. Large troid magnets provide magnetic fields to muon chambers

$$y = \frac{1}{2} \ln \left(\frac{E + p_z}{E - p_z} \right), \tag{2.4}$$

where E and p_z are the energy and z-component of the momentum of a given particle. The pseudo-rapidity, η, is defined using a polar angle θ as:

$$\eta = -\ln \left(\tan \frac{\theta}{2} \right), \tag{2.5}$$

which is an approximation of the rapidity at the massless limit.

The longitudinal component of energy and momentum of detected particles in the event is not conserved, while the transverse momentum of the initial partons is always zero. The conservation in the transverse direction is ensured so that usually we use transverse momentum $p_{\mathrm{T}} = p \sin\theta$ and transverse energy $E_{\mathrm{T}} = E \sin\theta$ to describe kinematical features of secondary particles. Secondary particles are assumed to be relativistic, of which the polar angle is described by η. The distance between two particles or two positions in the detector is defined in η-ϕ plane as:

$$\Delta R = \sqrt{\Delta\eta^2 + \Delta\phi^2}. \tag{2.6}$$

Particles produced in pp collisions can be identified by using a combination of sub-detectors. Figure 2.4 shows an example of the particle identification. Electrons[5] and

[5]The term electron refers to both electrons and positrons if not stated otherwise.

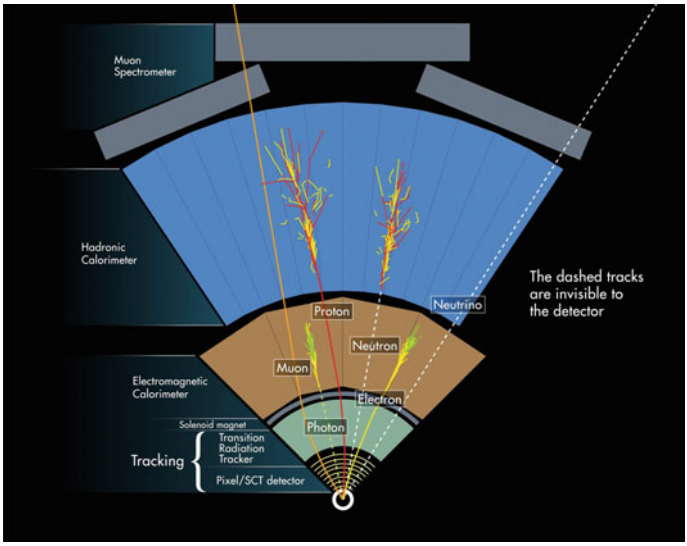

Fig. 2.4 An example of the particle identification with the ATLAS detector [2]

photons are detected as electromagnetic showers by the electromagnetic calorimeter: electron-induced showers can be distinguished from photon-induced ones by using inner detector information; hadrons deposit their energy at the hadronic calorimeter; muons can be detected at the outermost layer of the detector because of the long penetration length, and the momentum is reconstructed by both the inner detector and muon spectrometer; neutrinos do not interact with any detector materials, but consequently, existence of neutrinos are determined by the missing transverse energy, $E_{\mathrm{T}}^{\mathrm{miss}}$. The details of the reconstruction of each signature are described in Chap. 4.

The requirement for the ATLAS detector performance is summarized in Table 2.2. Each sub-detector is explained in the following sections.

2.2.1 Inner Detector

Inner detector plays an important role to reconstruct tracks of charged particles and the interaction point. The r-z view of the ATLAS inner detector (ID) is shown in Fig. 2.5. The cutting view of the ID system is illustrated in Fig. 2.6. The ATLAS ID system consists of three sub-detectors: silicon pixel detectors (Pixel); silicon micro-strip detectors (SCT); and transition radiation trackers (TRT). It can reconstruct the tracks and momenta of charged particles with $p_{\mathrm{T}} > 0.5$ GeV and $|\eta| < 2.5$ ($9^\circ < \theta < 171^\circ$). The 2 T magnetic field provided by the central solenoid magnet bends the charged particle, and its momentum is reconstructed from the curvature measured from the hits at each ID layer. The magnetic field is approximately uniform in $|z| < 2$ m, with small r and z dependency; see Fig. 2.7.

Table 2.2 Requirements for the ATLAS detector performance [6]

Sub-detector	Required resolution	Coverage	
		Measurement	Trigger
Tracking	$\sigma_{p_T}/p_T =$ $0.05\,\% p_T \oplus 1\,\%$	$\lvert\eta\rvert < 2.5$	–
EM calorimetry	$\sigma_E/E =$ $10\,\%/\sqrt{E} \oplus 0.7\,\%$	$\lvert\eta\rvert < 3.2$	$\lvert\eta\rvert < 2.5$
Hadronic calorimetry (jets)			
barrel and end-cap	$\sigma_E/E =$ $50\,\%/\sqrt{E} \oplus 3\,\%$	$\lvert\eta\rvert < 3.2$	$\lvert\eta\rvert < 3.2$
forward	$\sigma_E/E =$ $100\,\%/\sqrt{E} \oplus 10\,\%$	$3.1 < \lvert\eta\rvert < 4.9$	$3.1 < \lvert\eta\rvert < 4.9$
Muon spectrometer	$\sigma_{p_T}/p_T = 10\,\%$ at $p_T = 1$ TeV	$\lvert\eta\rvert < 2.7$	$\lvert\eta\rvert < 2.4$

The units of E and p_T are in GeV. Calorimeter and muon spectrometer are used also as trigger detectors. The character $\oplus$ indicates the orthogonal direct sum

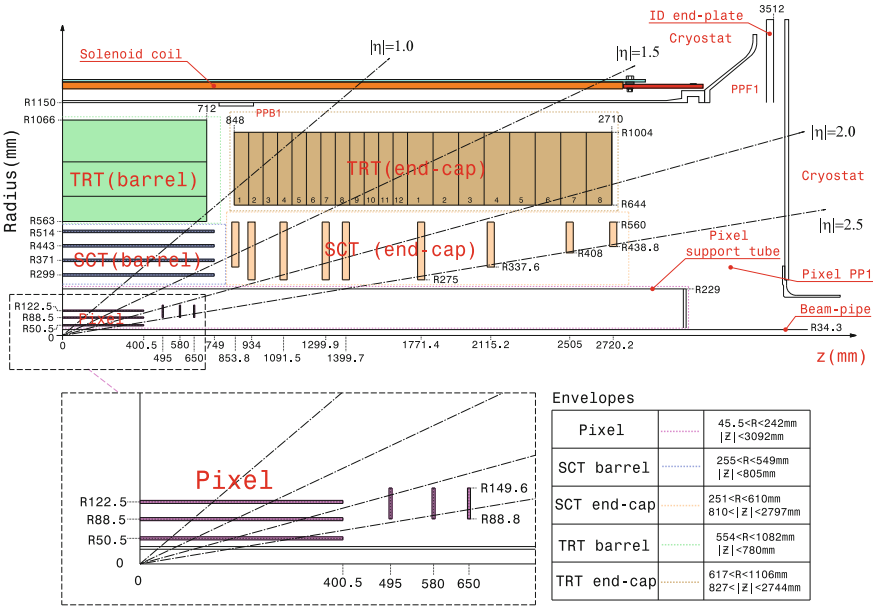

Fig. 2.5 The r-z view of a quarter section of the ATLAS inner detectors with their active dimensions and envelopes [6]. The *lower left part* shows the zoom-up view of the Pixel detector

High momentum resolution is required for the goal performance shown in Table 2.2. To perform the track reconstruction in the high pileup environment, a robust pattern recognition against the very large track density must be ensured. These are realized by high read-out granularity of the detectors. The precision measurements of

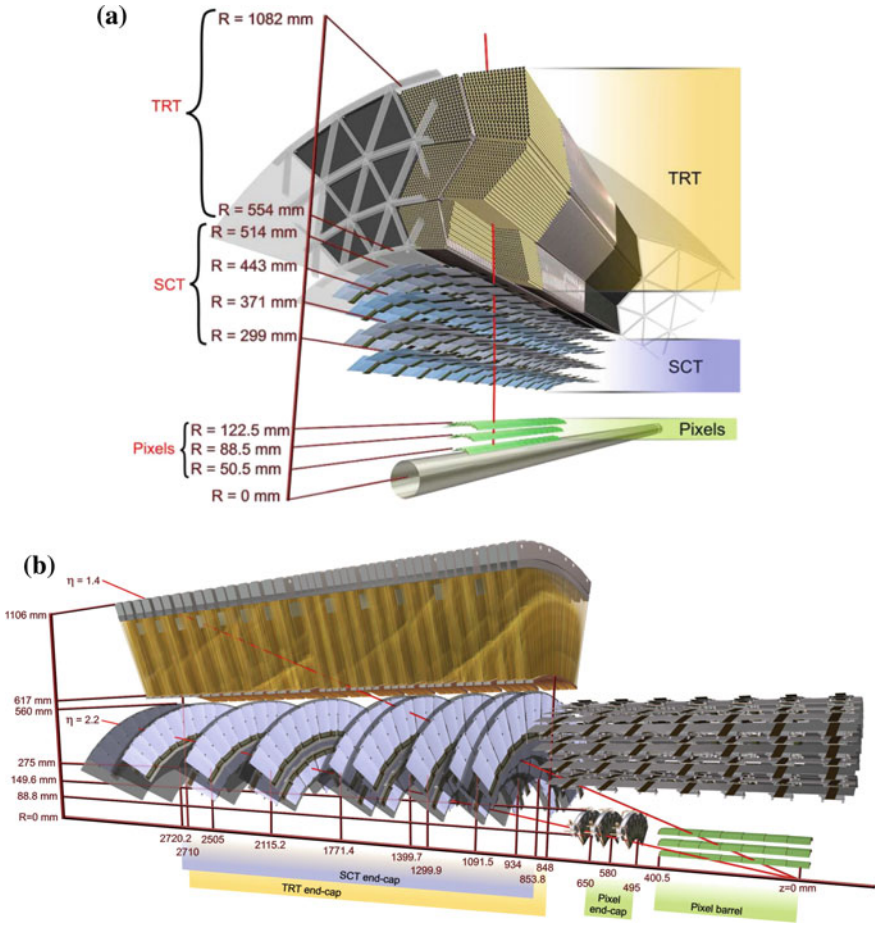

Fig. 2.6 Drawing of the ATLAS inner detector system at the barrel (**a**) and endcap (**b**) regions [6]. The infinite momentum lines for $\eta = 1.4$ and 2.2 are overlaid with *red lines* to (**b**)

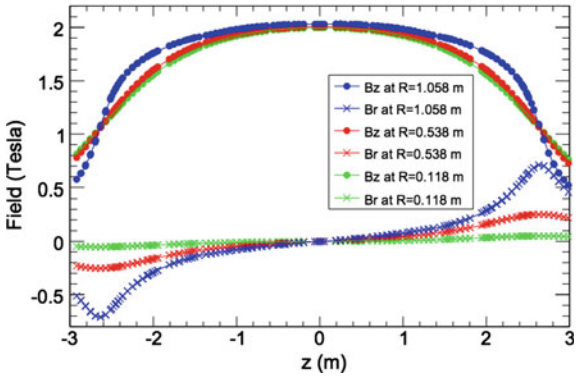

Fig. 2.7 r and z dependency of the radial (Br) and the axial (Bz) magnetic field in the inner detector cavity, at fixed azimuth [6]

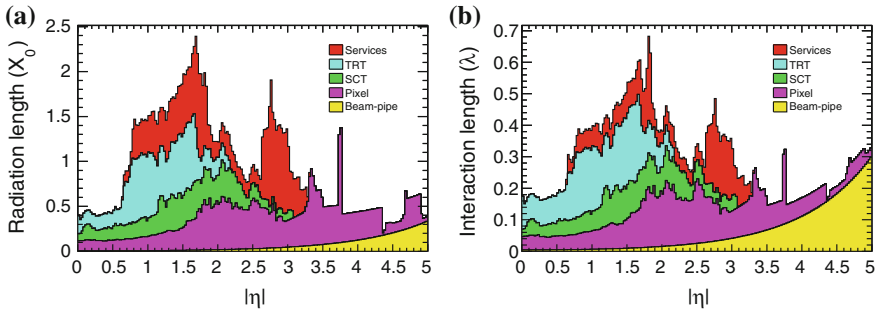

Fig. 2.8 The material distributions measured by the radiation length (**a**) and the nuclear interaction length (**b**) at the exit of the inner detector envelope as a function of $|\eta|$ for the ATLAS detector simulation [6]

charged particles make it possible to identify b-quark-induced jet, which is expected in the stop decay. Also electron identification against fake hadrons is performed for $|\eta| < 2.0$ ($15^\circ < \theta < 165^\circ$) using transition radiation photons at TRT.

The ID system is situated at the closest position to the beam pipe (about 5 cm) but the performance must be kept at the highest possible luminosity at the LHC and in high radiation environment. High-precision measurements of the detector alignments and amount of materials are also important to attain the required performance. Good understanding of the alignment for each sub-detector is made by a track-based algorithm minimizing a χ^2 based on track-hit residuals [7]. Material distribution measured by the radiation length (X_0)[6] and the nuclear interaction length (λ)[7] at the exit of the ID envelope are shown in Fig. 2.8.

The criteria and performance of the track and vertex reconstruction are explained in Sect. 4.1. Here, the technical details of the ID system are presented.

Pixel

The Pixel detector is placed at the innermost layer of the detector. In order to reconstruct primary and secondary vertices precisely, very high granularity of read-out cells and thinness of each Pixel layer are necessary. 1,744 oxygenated n-type silicon sensors with read-out pixel on the n^+-implanted side of the detector are installed. Nominal pixel sensor size is $50 \times 400\,\mu m^2$ with thickness of $250\,\mu m$ and the number of channels per sensor is 46,080.

[6]The radiation length X_0 is a characteristic of a material, related to the energy loss of electromagnetic interacting particles, which is defined as $E(x) = E_0 exp\left(-\frac{x}{X_0}\right)$, where $E(x)$ is a particle energy at the distance x in the material and E_0 is its initial energy i.e. X_0 is the path length required to reduce the energy of electromagnetic interacting particles by factor $1/e$ in a material.

[7]The nuclear interaction length λ is also a characteristic of a material, to describe the path length required to reduce the number of relativistic charged particles by the factor $1/e$ while they pass through a matter, which is defined as: $N(x) = N_0 exp\left(-\frac{x}{\lambda}\right)$, where $N(x)$ is the number of charged particles at the distance x, and N_0 is the initial number.

As shown in Fig. 2.5, there are three co-axial cylindrical layers of the Pixel at barrel region and three disk layers at both endcaps of the detector, which cover the range of $|\eta| < 2.5$ ($9° < \theta < 171°$). The innermost layer of the barrel Pixel detector, so-called *b*-layer, plays an important role to reconstruct secondary vertex. The intrinsic resolution is 10 μm in r-ϕ direction and 115 μm in z (r) direction for the barrel (endcap) region. The spacial resolution at each Pixel layer is measured using a test beam to be 12 μm in r-ϕ direction and it is found that approximately 80 % of the tracks have a single pixel hit.

SCT

There are four co-axial cylindrical SCT layers in the barrel region, and nine discs in both endcap regions, as shown in Figs. 2.5 and 2.6. Overall coverage of SCT is $|\eta| < 2.5$ ($9° < \theta < 171°$). A classic single-sided p-in-n technique with AC coupled read-out strip is employed for SCT. Total number of modules is 4,088 (2,112 in barrel and 1,976 in endcap region) and the number of read-out channels per each SCT module is 1,536. For noise suppression after radiation damage, the SCT must be kept at −5 to −10 °C.

In the barrel region, a strip pitch of 80 μm with daisy-chained 6 cm-long sensors are adapted. Each layer consists of two sensors at each on the top and bottom side, of which strips are rotated by ±20 mrad around the geometrical center as shown in Fig. 2.9. This layout makes it possible to determine the two dimensional space-point of a particle across the layer. In the endcap region, radial strips of constant azimuth with a mean pitch of about 80 μm are used. As with the barrel region, each module of nine discs has two sets of sensors glued back-to-back with a relative rotation of ±20 mrad to measure the two coordinates of the hit. The spacial resolution of SCT is measured using a test beam to be 16 μm in r-ϕ direction. The intrinsic accuracy

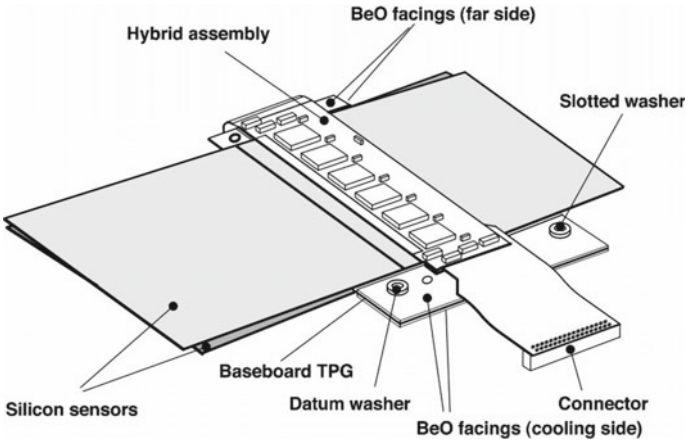

Fig. 2.9 Schematic view of a barrel SCT module [6]. Two silicon sensors are glued back-to-back on a thermal pyrolytic graphite (TPG) base-board which provides a high thermal conductivity path between the coolant and the sensors

in r-ϕ direction and z (r) direction for the barrel (endcap) region are 17 μm and 580 μm, respectively. It is confirmed that the resolution is not affected by irradiation.

TRT

TRT consists of 4 mm diameter polymide-made drift tubes. The tubes work as a cathode and 31 μm-diameter tungsten wires plated with 0.5–0.7 μm gold inside the tubes work as an anode, which are directly connected to front-end electronics and kept at ground potential. The gas component inside the tubes is 70 % Xe, 27 % CO_2 and 3 % O_2. The total number of read-out channels is approximately 351,000.

TRT covers the range of $|\eta| < 2.0$ ($15° < \theta < 165°$), with 73 layers in the barrel and 160 layers in the endcap region. The tube length is 144 cm in the barrel and 37 cm in the endcap region. The barrel tubes are laid in parallel with the beam pipe, side by side with an interval of 7 mm in each layer. There is small inefficient region of 2 cm at the center of tubes due to plastic insert to support the wires in each straw tube. In the endcap region, the TRT modules consist of two sets of individual wheels. For the inner region closer to the interaction point, twelve wheels with eight layers of straw tube strung by 8 mm pitch radially oriented are installed. For the outer set, eight wheels with eight straw layers are assembled with 15 mm pitch.

TRT can only measure space-points in r-ϕ direction, but charged particle with $p_{\mathrm{T}} > 0.5$ GeV traverses at least 36 tubes except for barrel-to-endcap transition region ($0.8 < |\eta| < 1.0$) which helps improving p_{T} resolution of tracks. The intrinsic resolution for each tube is 130 μm.

As the transition radiation material, 19 μm-diameter polypropylene fibers (barrel) and 15 μm-thick polypropylene radiator foils separated by a polypropylene net (endcap) are inserted between tubes. Detection of transition radiation photon caused by materials with different refractive indices helps to distinguish electron tracks from hadrons for wide range of electron energy of $0.5 < E < 200$ GeV. The energy of transition radiation photon is proportional to $\gamma = E/m$, where E and m are energy and mass of the charged particles, respectively. Transition radiation photon is absorbed by Xe inside tubes and the signal is detected at TRT. Figure 2.10 indicates the high-threshold hit probability as a function of γ derived by 7 TeV collision data with ATLAS in 2010. It is seen that response from electron is significantly higher than that for hadrons for the same momentum. Seven to ten high-threshold hits from transition radiation are expected by electrons with $E > 2$ GeV.

2.2.2 Calorimetry

In this thesis, the calorimeter services are used to reconstruct the electron and hadronic jets from the stop decay. Good energy resolution of the electromagnetic calorimeter even in the low-E_{T} region is required to reconstruct the soft electron, which is the kinematic feature of the target signal. Signals at the calorimeters are also used to reconstruct the $E_{\mathrm{T}}^{\mathrm{miss}}$. The ATLAS sampling calorimeter system is illustrated in Fig. 2.11. It covers the range of $|\eta| < 4.9$ ($1° < \theta < 179°$) by using several

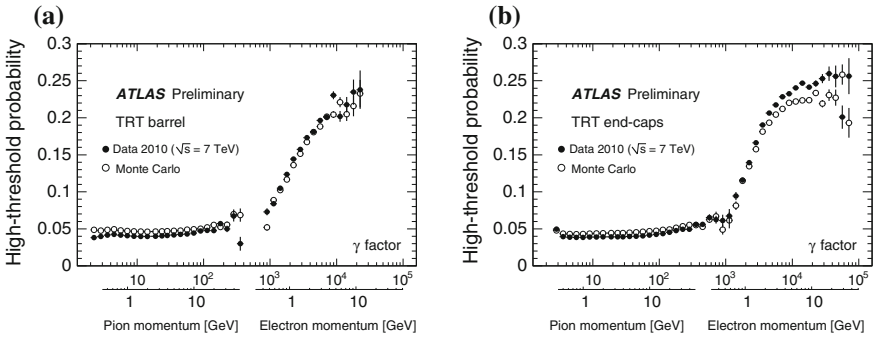

Fig. 2.10 The probability of a TRT high-threshold hit as a function of $\gamma = E/m$, for the TRT barrel (**a**) and endcap (**b**) regions, as measured in 7 TeV collision data collected in 2010 with the ATLAS detector [8]

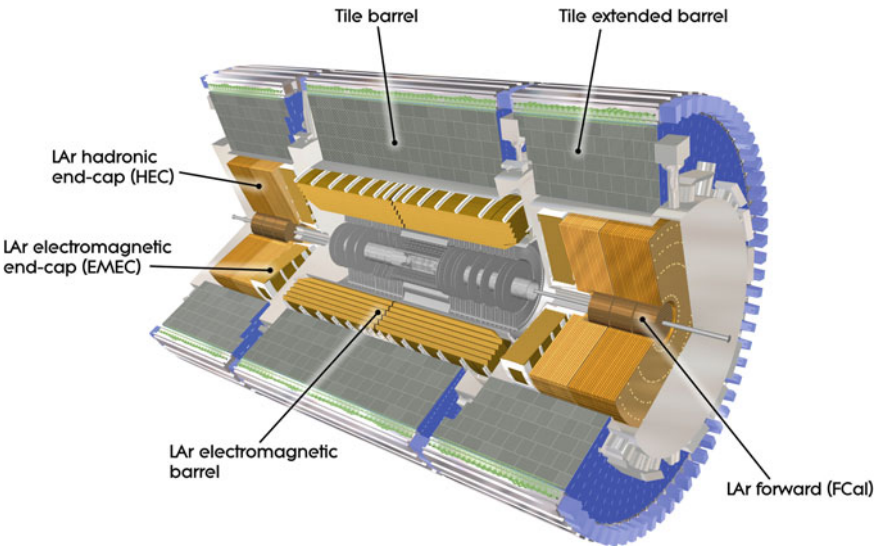

Fig. 2.11 The overview of the ATLAS electromagnetic and hadronic calorimeter [6]. It consists of lead-LAr electromagnetic calorimeter in the barrel and endcap regions (endcap LAr calorimeter is called as EMEC), hadronic endcap LAr calorimeter (HEC), barrel sampling hadron calorimeter using steel absorber and tile scintillator, and forward LAr calorimeter (FCal)

techniques suited to the requirements at each η range. It consists of electromagnetic (EM) Liquid-Argon (LAr) calorimeter, hadronic tile calorimeter, hadronic endcap LAr calorimeter (HEC) and forward LAr calorimeter (FCal).

It is important that hadron jets must deposit all their energy inside the calorimetry service and not be detected in the muon chamber. The amount of materials for the EM calorimeter using radiation length is shown in Fig. 2.12 and that for whole calorimetry system using nuclear interaction length is shown in Fig. 2.13. Total active thickness

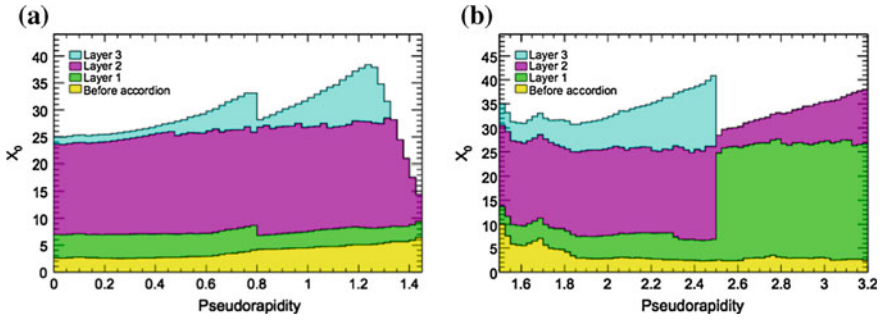

Fig. 2.12 The amount of materials at each service at the EM calorimeter divided into Layer1, Layer2 and Layer3 using radiation length as a function of η at barrel (**a**) and endcap (**b**) region, respectively [6]

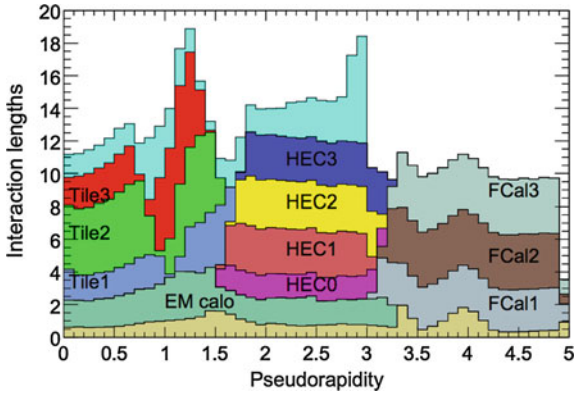

Fig. 2.13 The amount of materials of each the ATLAS calorimeter module as a function of η using nuclear interaction length [6]

of the EM calorimeter is greater than $24X_0$. At least 10λ is provided at the exit of the hadronic calorimeter in the whole η region.

Calorimeters are synchronized to the LHC clock every 25 ns at the trigger level to identify the bunch crossing. Pulse shape of the collected signals is recognized and cell energy is reconstructed by the optimal filtering algorithms [6]. Criteria to reconstruct e/γ and hadron jets are explained in Sects. 4.2 and 4.5. Here, only the technical details of ATLAS calorimeter system are presented.

EM LAr Calorimeter

Lead absorber and active LAr detector are employed for the EM calorimeter, with an accordion geometry to perform complete ϕ symmetry without azimuthal crack. It consists of two sets of barrel detector and two endcap detectors (EMECs) as shown in Fig. 2.11.

In the LAr calorimeters (EM and hadronic endcap calorimeter), ionization electrons produced by passing charged particles drift to electrodes and produce electrical currents proportional to the deposited energy. Signals are sent to the front-end board and the pre-amplifier is applied. LAr calorimeter has a better energy resolution in

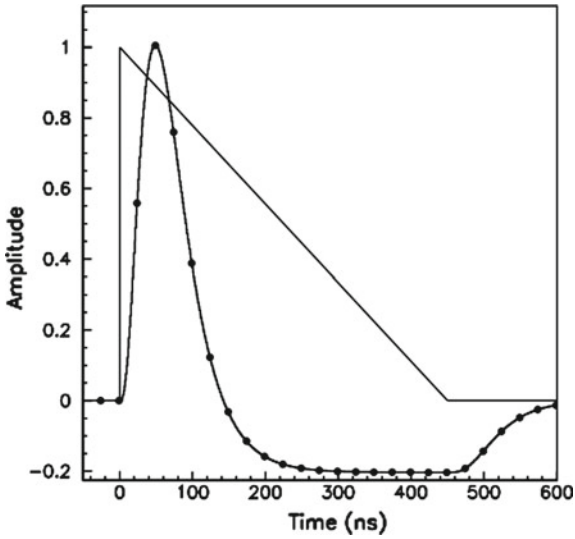

Fig. 2.14 An example of the bipolar pulse shape in the ATLAS LAr calorimeter (barrel EM calorimeter) [6]. The sampling points every 25 ns are also shown

comparison with scintillator, but output triangular pulse has the base time of typically 600 ns, while that of signals from the Tile calorimeter is about 200 ns. Consequently, the LAr calorimeter is likely to be affected by the 'out-of-time pileup' from the other bunch crossing. To discriminate 'in-time' signals from the background, pulse shape from the LAr calorimeter is translated to be bipolar as shown in Fig. 2.14 using analogue filter, which allows the negative energy in the cell for the out-of-time background. The signals are then sampled at the LHC clock by analogue technique and sent to the ADC for the trigger (see Sect. 2.2.4). Only events accepted by the hardware-based trigger are read out and amplified by the optimal readout gain. Signals from all calorimeters are sent to the back-end system. At the back-end system, optimal filtering is applied to signals to reconstruct the energy of each calorimeter cell.

The barrel EM calorimeters cover $|\eta| < 1.475$ ($26° < \theta < 164°$). There is only small dead region at $z = 0$ by $\sim$4 mm between two detectors for cabling. They are enclosed in cryostat vessels which maintain the LAr temperature at 88 K. Each module has three layers so-called Layer1, Layer2 and Layer3, from inside to outside. The depth of each layer is shown in Fig. 2.12a using the radiation length X_0. Schematic diagram of the barrel EM calorimeter positions is shown in the top panel of Fig. 2.15. The actual depth for each layer is optimized according to $|\eta|$ to fulfill uniform X_0 values with respect to η. Figure 2.16 shows a module of the barrel EM calorimeter. The figure shows that higher granularity of read-out cells along η direction at Layer1 is adapted (size of one read-out cell is $\Delta\eta \times \Delta\phi = 0.025/8 \times 0.1$) to measure η of reconstructed e/γ precisely. Most of the energy of the electromagnetic shower is dropped at Layer2, which has the longest depth among three layers. It has 8 times coarser read-out granularity in η direction than Layer1, but is divided into four sub-modules in ϕ direction ($\Delta\eta \times \Delta\phi = 0.025 \times 0.025$). Layer3 is used to

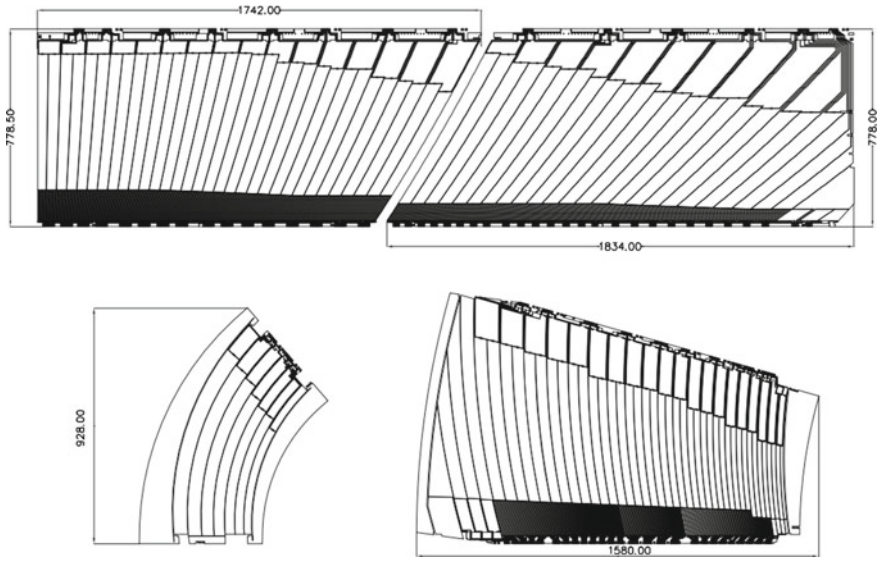

Fig. 2.15 Layout of the EM calorimeter layers, which is optimized to perform approximately the same radiation length at each layer in all η range [6]. The two top electrodes are for the barrel and the two bottom are for the endcap *inner* (*left*) and *outer* (*right*) wheels. Dimensions are in mm

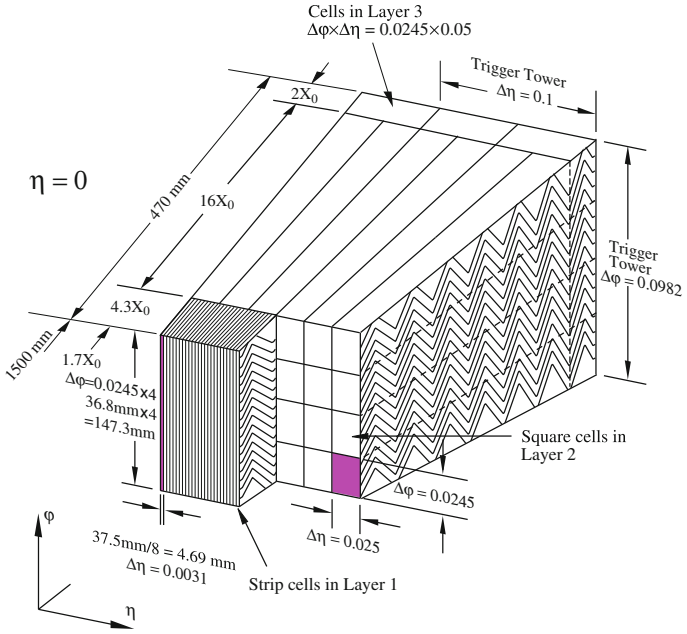

Fig. 2.16 Drawing of a module of the barrel EM calorimeter [6]

measure the tail of electromagnetic shower and to distinguish e/γ from hadron jets. Layer3 has the coarser read-out granularity in η direction by factor 2 than Layer2 ($\Delta\eta \times \Delta\phi = 0.05 \times 0.025$).

The EMEC calorimeters at each side of the barrel EM calorimeters cover the range of $1.375 < |\eta| < 3.2$ ($5^\circ < \theta < 28^\circ$ and $152^\circ < \theta < 175^\circ$). Each EMEC has two co-axial wheels. Inner wheel covers $2.5 < |\eta| < 3.2$ ($5^\circ < \theta < 9.4^\circ$ and $171^\circ < \theta < 175^\circ$) and outer wheel covers $1.375 < |\eta| < 2.5$ ($9^\circ < \theta < 28^\circ$ and $152^\circ < \theta < 171^\circ$). There is a 3 mm gap region between two wheels at $|\eta| = 2.5$ for cabling. All wheels are further divided into 8 wedge-shaped modules. Illustrations of the inner and outer EMEC module are shown in bottom two panels of Fig. 2.15. As with the barrel region, the precision region of EMEC calorimeter (which can match the ID system: $1.5 < |\eta| < 2.5$) is divided into 3 layers in depth as shown in Fig. 2.12b. The front layer is segmented with strips along the η direction. The $\Delta\eta$ is optimized for each η region (at most 0.025 at the core region), and $\Delta\phi = 0.1$. The size of the read-out cell in the middle layer is $\Delta\eta \times \Delta\phi = 0.025 \times 0.025$, except for barrel-to-endcap and endcap-to-forward boundaries. The back layer has a twice coarser granularity in η with respect to the middle layer ($\Delta\eta \times \Delta\phi = 0.05 \times 0.025$). The other regions ($|\eta| < 1.5$ and $2.5 < |\eta| < 3.2$) are divided into two longitudinal layers (see Fig. 2.12) and have a coarser transverse granularity ($\Delta\eta \times \Delta\phi = 0.1 \times 0.1$).

The transition region between the barrel and endcap EM calorimeters, $1.37 < |\eta| < 1.52$, has a large amount of material in front of the first calorimeter layer, ranging from $5X_0$ to $10X_0$. To improve energy measurement accuracy in this region, the LAr pre-sampler detectors are located in front of EM calorimeters, covering the range of $|\eta| < 1.52$ ($25^\circ < \theta < 155^\circ$) (barrel) and $1.5 < |\eta| < 1.8$ ($19^\circ < \theta < 25^\circ$ and $155^\circ < \theta < 161^\circ$) (endcap). The read-out granularity of the pre-sampler calorimeter is $\Delta\eta \times \Delta\phi = 0.025 \times 0.1$ and thickness is 11 mm (5 mm) for barrel (endcap).

The energy resolution of the EM calorimeter is measured using a test beam. The resolution is described after noise subtraction by the following formula:

$$\frac{\sigma\,(E)}{E} = \frac{a}{\sqrt{E\ (\text{GeV})}} \oplus b, \tag{2.7}$$

where a is the statistical term and b is the constant term to take into account the local dependency of the pedestal of each calorimeter. The performance of barrel EM calorimeter is described by $a = (10.1 \pm 0.4)$ % and $b = (0.2 \pm 0.1)$ %, which is compatible with the target performance described in Table 2.2.

Hadronic Tile Calorimeter

ATLAS uses steel absorber and scintillating tile as the active material for the barrel hadronic calorimeter. The tile calorimeter consists of one long module covering $|\eta| < 1.0$ ($40^\circ < \theta < 140^\circ$) and two extended modules covering $0.8 < |\eta| < 1.7$ ($21^\circ < \theta < 48^\circ$ and $132^\circ < \theta < 159^\circ$). They are divided azimuthally to 64 sub-modules. It is segmented into three layers in depth, by approximately 1.5λ, 4.1λ and 1.8λ for barrel, and 1.5λ, 2.6λ and 3.3λ for extended barrel as shown in Fig. 2.13.

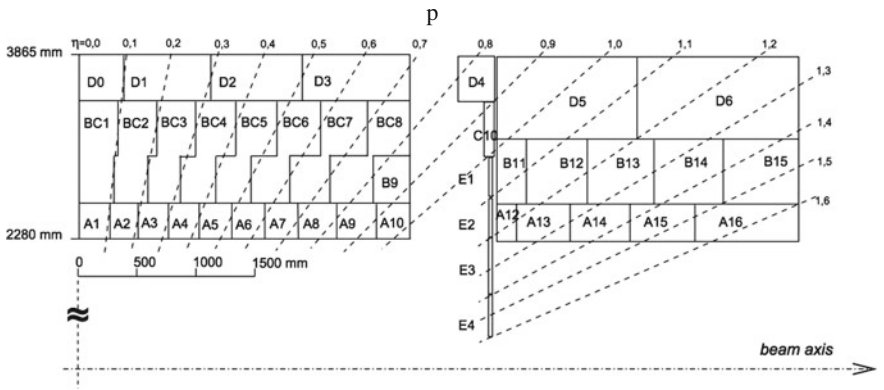

Fig. 2.17 Segmentation in depth and η of the tile calorimeter modules in the central (*left*) and extended (*right*) barrels [6]. The bottom of the picture corresponds to the inner radius of the tile calorimeter. The tile calorimeter is symmetric with respect to the interaction point

Segmentation of the hadronic tile calorimeter is illustrated in Fig. 2.17. Each cells have the dimensions of $\Delta\eta \times \Delta\phi = 0.1 \times 0.1$ for first and second layers and 0.1×0.2 for third layer.

Scintillation light is collected by the wavelength-shifting fibers [6] placed in contact with the tile edge and converted to a longer wavelength. Each fiber collects light from tiles located at one or two radial depths in the calorimeter and transmits it to the photomultiplier as shown in Fig. 2.18. Signals are transformed to unipolar pulse shape and amplified using analogue functions, and sent to the L1 trigger (see Sect. 2.2.4). Signals are digitalized every 25 ns by the ADC and only events passing the L1 trigger are recorded.

The fractional resolution $\sigma(E)/E$ of standalone tile calorimeter is measured using an isolated pion test beam. It is parameterized by Eq. (2.7) and found to be $a = (56.4 \pm 0.4)$ % and $b = (5.5 \pm 0.1)$ % at $\eta = 0.35$. It is improved to $a = (52.0 \pm 1.0)$ % and $b = (3.0 \pm 0.1)$ % by taking a combination with the EM calorimeter information.

Hadronic Endcap LAr Calorimeter (HEC)

In the endcap region, LAr calorimeter is adapted for the measurement of hadrons. Two wheels are located at both endcaps covering $1.5 < |\eta| < 3.2$ ($5° < \theta < 25°$ and $155° < \theta < 175°$) directly behind EMEC calorimeter sharing the LAr cryostat. Each wheel consists of 32 wedge-shaped modules. Each module is divided into two segments in depth, thus, there are 4 layers for each endcap. 25 mm (50 mm) copper plates laid in parallel are used for front (back) module as absorber. Number of copper plates is 24 (16) for the front (back). The 8.5 mm gap between copper plates provides the LAr active medium for the sampling calorimeter. The detector thickness of each HEC layer in λ is shown in Fig. 2.13. Total thickness of the HEC is about 10λ.

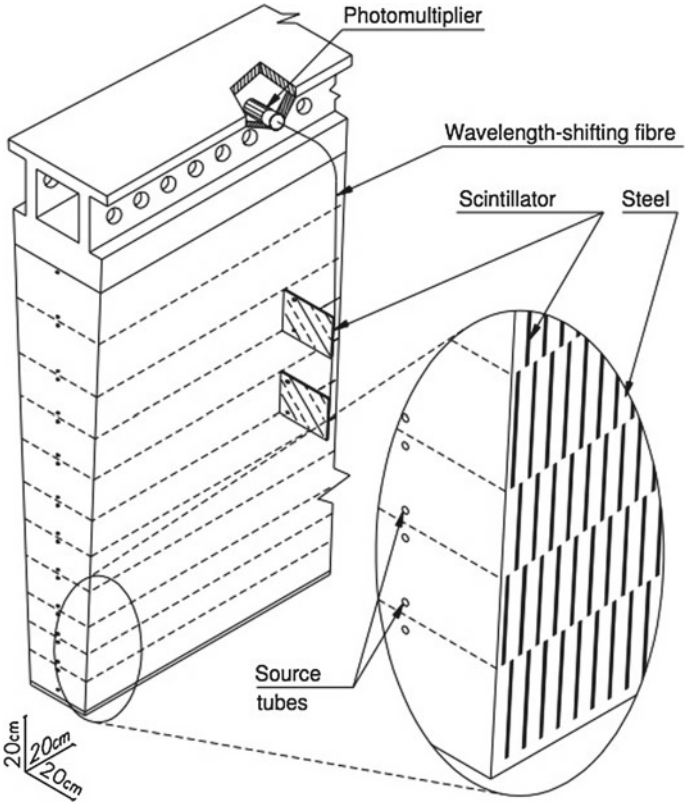

Fig. 2.18 Schematic illustration of the mechanical assembly and the optical readout of the ATLAS hadronic tile calorimeter [6]

The read-out granularity of the HEC is $\Delta\eta \times \Delta\phi = 0.1 \times 0.1$ for $1.5 < |\eta| < 2.5$ and 0.2×0.2 for $2.5 < |\eta| < 3.2$. The resolution of the HEC is measured using a pion test beam with the same parameters as Eq. (2.7), resulting in $a = (70.6 \pm 1.5)\,\%$ and $b = (5.8 \pm 0.2)\,\%$. At the transition region to FCal ($|\eta| = 3.2$), $a \simeq 81$–$85\,\%$ is found. It is worse than the other regions, but meets well the designed value of $a = 100\,\%$ in Table 2.2.

Forward LAr Calorimeter (FCal)

Another set of layers of calorimeter are arranged close to the beam axis to measure the secondary particles with small scattering angle. Figure 2.19 illustrates a schematic diagram for positions of the FCal. It covers the range of $3.1 < |\eta| < 4.9$ ($1^\circ < \theta < 5^\circ$ and $175^\circ < \theta < 179^\circ$). It consists of three modules and the depth is approximately 10λ as shown in Fig. 2.13. First module, made of copper, is optimized to electromagnetic measurements. The other two modules are made of tungsten, which measure hadronic interactions. The gap between materials as LAr active medium is 0.25 mm to avoid the effect of high particle flux and the radiation damage according to the

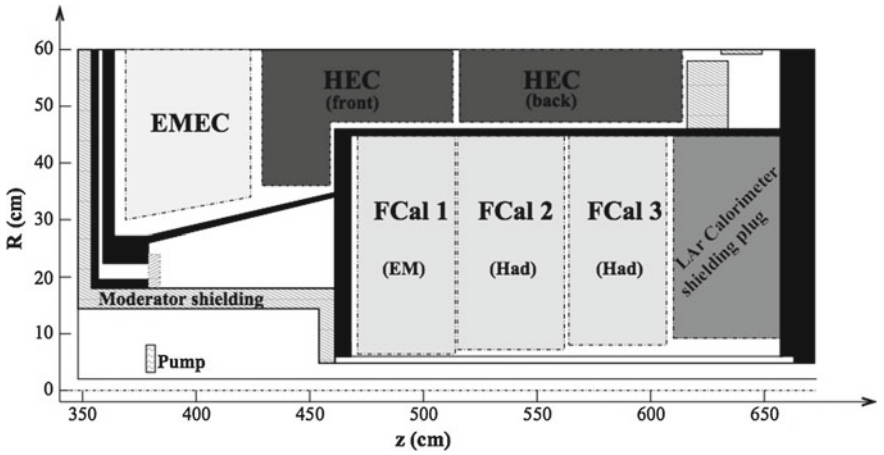

Fig. 2.19 Schematic diagram of three forward LAr calorimeters located in the endcap cryostat [6]. FCal1 is used for electromagnetic measurements while FCal2 and FCal3 are used for hadronic measurements. Materials in front of the forward calorimeter and shielding plug behind that are also shown. *Black region* indicates structure of the cryostat

small polar angle. In order to reduce the amount of neutron albedo in the inner detector cavity, the front face of the FCal is away from EM calorimeter front face by about 1.2 m.

The resolution of the FCal is estimated using a test beam. Two ways are tested. The first one uses single weight per module (flat weight) yielding $a = (28.5 \pm 1.0)\,\%$ and $b = (3.5 \pm 0.1)\,\%$ for electrons and $a = (94.2 \pm 1.6)\,\%$ and $b = (7.5 \pm 0.4)\,\%$ for pions, respectively, where a and b are defined in Eq. (2.7). The second one is more sophisticated technique using radial weights with fine transverse segmentation, improving a from 94 to 70 % and b from 7.5 to 3.0 % for the hadron measurement. The measured resolution of the FCal is acceptable in comparison with the designed value described in Table 2.2.

2.2.3 *Muon Spectrometer*

Muon spectrometer is designed to measure wide range of muon momenta from a few GeV to about 3 TeV. Figure 2.20 shows the ATLAS muon detectors, which consist of four types of sub-detectors: monitored drift tubes (MDT), cathode strip chambers (CSC), resistive plate chambers (RPC) and thin gap chambers (TGC). Large and small chambers are located sided by side at each layer in both barrel and endcap regions, leading to a region overlapping in ϕ in order to gain the geometrical acceptance, as shown in Fig. 2.20a for the barrel region. MDT and CSC are used for precision measurement, while RPC and TGC which are synchronized to the LHC clock to

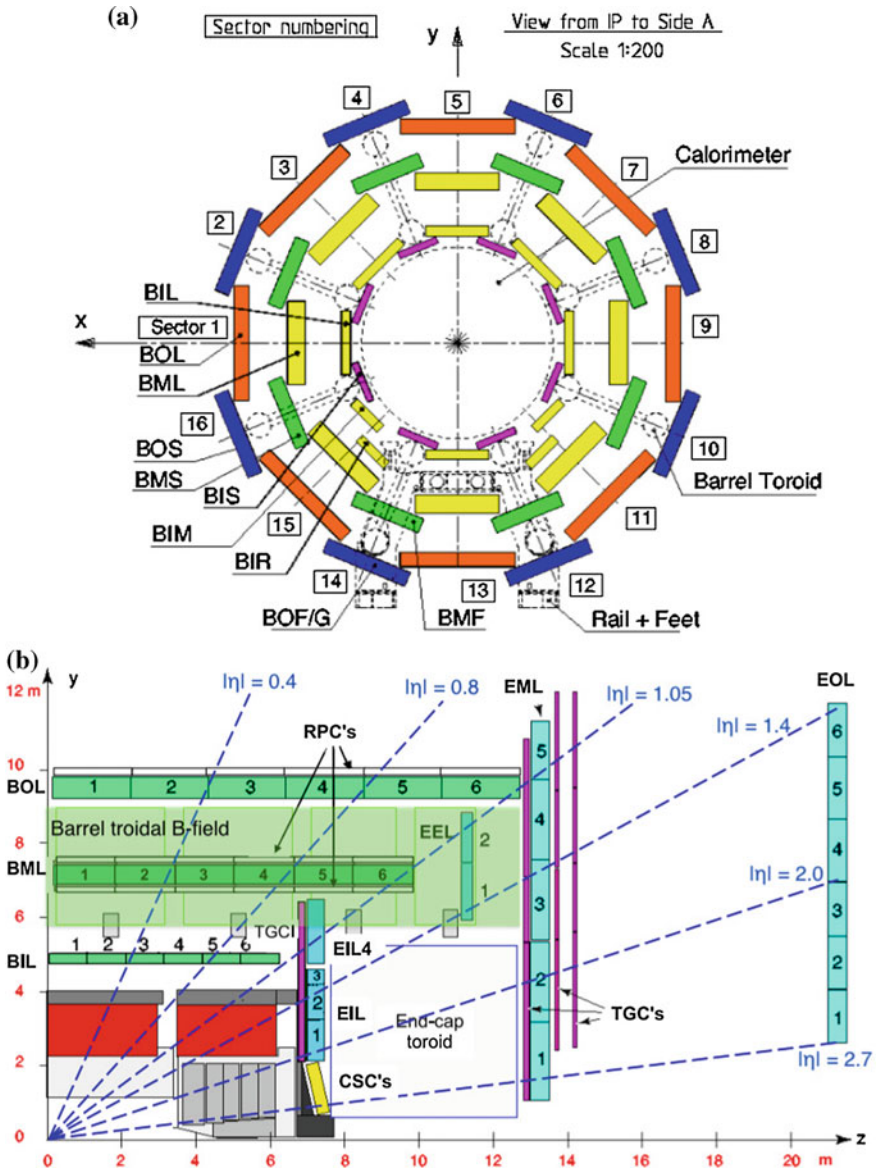

Fig. 2.20 **a** Cross section of the ATLAS barrel muon system perpendicular to the beam axis [6]. In the barrel region, eight-folded ϕ symmetric structure is employed. Large and small chambers are located side by side, which lead to a region overlapping in ϕ to gain the acceptance. There are two feet to hold the detector up at sector 11–12 and 14–15, which lead to an acceptance loss. **b** r-z view of the ATLAS muon system [6]. *Green* and *blue colors* show barrel and endcap MDTs, respectively; *yellow* chamber is CSC; *white* chambers RPCs; and *magenta* TGCs. The barrel toroidal magnetic field and the endcap troidal magnetic field are indicated with *light green* and *blue shades*, respectively

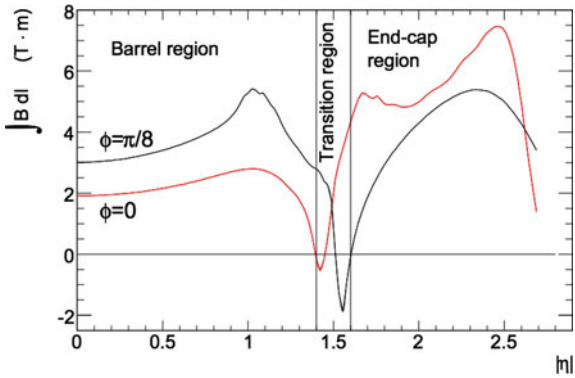

Fig. 2.21 Predicted magnetic field integral from innermost to outermost MDT layer in one troid octant, as a function of $|\eta|$, corresponding to the azimuthal angle $\phi = \pi/8$ (*black*) and $\phi = 0$ (*red*) [6]

identify the bunch crossing are used for the trigger. The muon system is operated in the magnetic field, of typically 0.5 T provided by the barrel large toroidal magnet in $|\eta| < 1.4$ ($28° < \theta < 152°$), and 1 T by the endcap troidal magnets for both endcaps of the detector in $1.6 < |\eta| < 2.7$ ($8° < \theta < 23°$ and $157° < \theta < 172°$). In the transition region ($1.4 < |\eta| < 1.7$), magnetic deflection is caused by a combination of barrel and endcap fields, as shown in Fig. 2.21. The magnetic fields forming 8-fold symmetry in ϕ are mostly orthogonal to muon directions. The muon track is bent by the magnetic field in η direction and its momentum and position are reconstructed using hits at muon chambers. The distance between the inner and outer layers of MDT is about 5 and 14 m in barrel and endcap, respectively, as shown in Fig. 2.20b. Long baseline of the measurement leads to a better p_T-resolution for high-p_T muons. By taking a combination with ID tracks, more precise reconstruction of muon can be made, in particular in the low-p_T region. The muon identification criteria is described in detail in Sect. 4.3.

MDT

In the region $|\eta| < 2.7$ ($8° < \theta < 172°$), precision measurement of tracks is performed with MDT. MDT consists of 1,088 chambers and 339,000 read-out channels. There are three MDT layers both for the barrel and endcap regions as shown in Fig. 2.20. Each layer consists of 2×4 (inner MDT layer) or 2×3 (middle and outer MDT layer) drift-tube walls as illustrated in Fig. 2.22a. The diameter of a drift tube is ~30 mm and the gas component inside the tube is 93 % Ar, 7 % CO_2 and less than 1000 ppm H_2O. Small mixture of water is foreseen to improve high-voltage stability. The effect of water on the drift behavior is negligible. The electrons from ionization are collected at the central tungsten-rhenium wire with a diameter of 50 μm. Maximum drift time is 700 ns. By making segments using combinations of multiple tubes per each layer as shown in Fig. 2.22b, it performs very high spacial resolution of 35 μm, whereas average resolution of individual tubes is 80 μm. MDT can measure only in z (r) direction for barrel (endcap). Secondary coordinate information (ϕ) is provided by RPC for barrel and TGC for endcap.

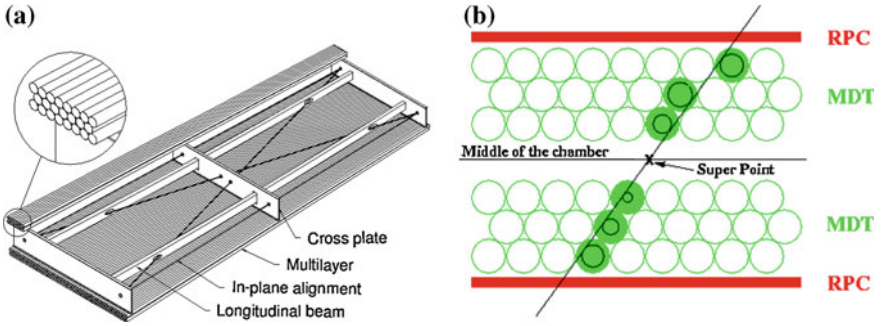

Fig. 2.22 **a** The viewing of a MDT module [6] and **b** an example to reconstruct muon segment [9]. Two sets of three drift tube walls form one module (for middle and outer MDT layer). Drift tubes are shown in *green* (*light gray*) outlined circles in (**b**). The charged particle trajectory is shown as the *straight black line* and the drift *circles* are shown in *black*. A linear fit on the drift circles is performed and the segment of the muon candidate is reconstructed

CSC

The limit for safe operation of the MDT is 150 Hz/cm^2, which will be exceeded for $|\eta| > 2.0$ ($\theta > 165°$ and $\theta < 15°$) at the innermost layer. To cope with high muon rate in the forward region of $2.0 < |\eta| < 2.7$, CSC is used for the innermost layer of the muon system, which can be operated safely with a counting rate of 1000 Hz/cm^2. There are 32 CSC chambers and the number of read-out channels is 31,000. Same as the MDT, CSC is segmented into large and small chambers side by side in ϕ direction. CSC is a multi-wire proportional chamber using cathode planes segmented into strips in orthogonal directions. This technique allows to measure both coordinates of muon tracks. Anode wire diameter is 30 μm and wire pitch is 2.5 mm. The cathode strip pitch is 5.31 and 5.56 mm for large and small chambers, respectively. The gas mixture is Ar : CO_2 = 80 : 20. The spacial resolution is 40 μm in r direction and 5 mm for R-ϕ direction. The time resolution is 7 ns.

RPC

The muon trigger chambers in the barrel region consist of three layers of RPC as shown in Fig. 2.20b. There are two RPC layers inside and outside of the middle MDT layer and one RPC layer outside of the outer MDT layer. RPC is a no-wire gas detector. Number of chambers is 544 and number of read-out channels is 359,000. The gas is enclosed between two phenolic-melaminic plastic laminate resistive plates located in parallel to each other at a distance of 2 mm. The gas mixture is 94.7 % $C_2H_2F_4$, 5 % Iso-C_4H_{10} and 0.3 % SF_6. The electric field between the plates allows avalanches to form along the ionizing tracks towards the anode. The anode strips consist of 17 μm-thin copper on PET foil. Each strip has a width of 25–30 mm. Each RPC layer consists of two sub-layers, which have strips to measure η and ϕ, respectively. Spacial resolution is 1 mm, but the frequency response of the gas-amplifiers has a maximum at 100 MHz and a 60 MHz bandwidth. A time resolution of RPC is 1.5 ns.

TGC

TGC is a multi-wire proportional chamber covering $1.05 < |\eta| < 2.7$ ($8° < \theta < 39°$ and $141° < \theta < 172°$) in the endcap region. The gas mixture is CO_2 : n-pentane = 55 : 45. The wire pitch is 1.8 mm and the wire-to-cathode pitch is 1.4 mm, resulting in a spacial resolution of 2–6 mm. Number of chamber is 3,588 and number of read-out channels is 318,000. As shown in Fig. 2.20b, one layer of TGC is located in the innermost MDT layer (TGC I) and three TGC layers are in the middle MDT layer. Three TGC layers in the middle are used as trigger chambers in $|\eta| < 2.4$ ($\theta > 10°$ and $\theta < 170°$), because of the fast response (20 ns of the maximum drift time) and good time resolution (4 ns). Two-dimensional read-out is performed by the anode wires (in r) and the graphite cathode strips (in ϕ).

2.2.4 Trigger and Data Acquisition System

As described in Sect. 2.1, the LHC has been operated typically with bunch spacing of 50 ns in 2012, corresponding to 20 MHz bunch crossing frequency. Concerning the pileup, we expect $O(1)$ GHz of pp collision rate. However, due to the limit of the computer facilities e.g. the disc access and the storage spaces, all of events produced in pp collisions cannot be recorded. Therefore, we need to apply tight event selection to collect rare signals against large background during data taking. This scheme is called trigger system. The acceptable trigger and data rate in 2012 was 700 Hz and 1 GB/s [10].

To cope with this challenging task, ATLAS employees three-level trigger system which consists of Level 1 (L1), Level 2 (L2) and Event Filter (EF) with increasing complexity and accuracy. The L2 and EF are collectively referred to as the Higher Level Trigger (HLT). The schematic view of the ATLAS trigger and data acquisition system is shown in Fig. 2.23. There are various event topologies that one wants to record depending on physics channels analyzed with ATLAS, so a signature-based trigger algorithm using e/γ, hadronic-decaying τ leptons, hadron jets, muons, and missing transverse energy, $E_{\mathrm{T}}^{\mathrm{miss}}$, is adapted. Combinations of each signature at the trigger level allow to define many variations of trigger logics based on event topology in parallel. Each logic is so-called a 'trigger chain'. The band width is assigned to each trigger chain. Trigger chains exceeding the acceptable rate are pre-scaled. Pre-scaling factors can be determined individually and be changed during the data taking period, according to the beam situation of the LHC. For example, the trigger chain `EF_mu4T`, requiring at least one muon with $p_{\mathrm{T}} > 4$ GeV, worked with high pre-scaling factor corresponding to 1.5 Hz of data-taking rate in 2012, in order to check the performance for the low-p_{T} muon signature.

In the LHC run1, the first running period of the experiment, there were some problems with the trigger system. I had applied some improvements on the muon reconstruction algorithm at the trigger level as an expert of the trigger system, as shown in Appendix G. My improvements suppressed the trigger rate while keeping

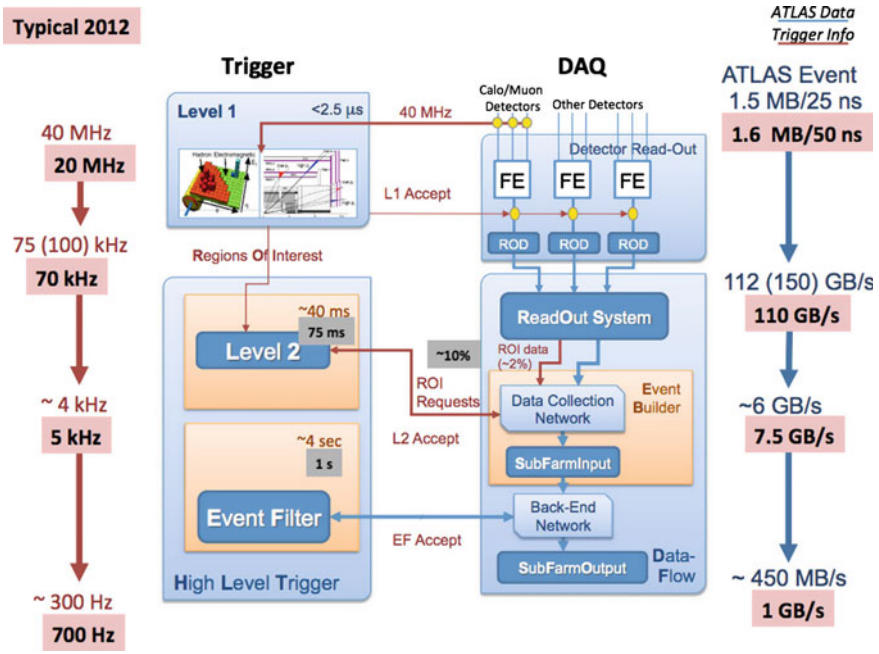

Fig. 2.23 The schematic view of the ATLAS trigger and data acquisition system [11]. The ATLAS physics data flow is indicated by *blue lines* and trigger information by *red lines*. In 2012, typical *pp* collision rate was 20 MHz corresponding to the output data stream of 1.6 MB/50 ns. The ATLAS three-level trigger system, applying tight event selection during the data taking, reduces the data taking rate to 700 Hz and 1 GB/s

the efficiency to events containing muons. It contributed to the ATLAS data taking in the LHC run1 with high efficiency of greater than 90 %.

The L1 Trigger

At the L1, fast and rough reconstruction of each signature is performed, using electromagnetic and hadronic calorimeters and fast muon trigger chambers (TGC and RPC). The L1 trigger defines the Region of Interest (RoI) and passes it to the HLT. By reading the signals from each sub-detector only around the RoI, faster reconstruction at the HLT can be realized. Acceptable output rate at the L1 in 2012 was 70 kHz and required latency was less than 2.5 μs.

The e/γ candidates are reconstructed in the electromagnetic calorimeter based on 'trigger tower's with rough segmentation of the EM calorimeter in η and ϕ directions i.e. $\Delta\eta \times \Delta\phi = 0.1 \times 0.1$ and no segmentation in depth for faster read-out time; see Fig. 2.24. Combinations of 2×2 towers in which at least one of the four possible two tower sum (2×1 or 1×2) of the nearest neighbor towers exceeds predefined energy threshold form the RoI.

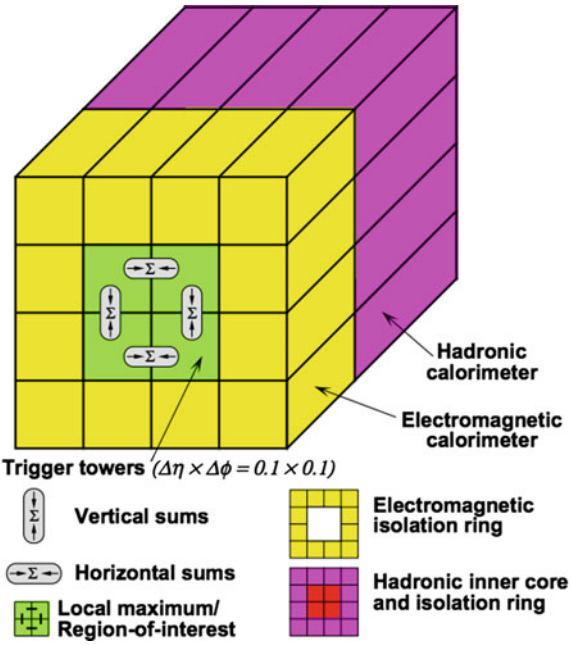

Fig. 2.24 The L1 electron/photon reconstruction algorithm [6]

Jet reconstruction algorithm at L1 works with jet elements which are the sum of 2×2 trigger towers in the EM calorimeter added to 2×2 trigger towers at hadronic calorimeter. The E_{T} summed over 2×2, 3×3 or 4×4 towers of hadronic calorimeter is compared with predefined E_{T} threshold and the jet candidate passing the threshold is defined as an RoI.

Missing transverse energy is reconstructed by vector-sum of all clusters reconstructed in the calorimeter. Correction from muons is not applied.

For muon candidates, RPC and TGC calculate p_{T} of muon tracks roughly using the predefined look-up-table from hit pattern at each detector layer. The typical dimensions of the muon RoI is $\Delta\eta \times \Delta\phi = 0.1 \times 0.1$ (0.03×0.03) for RPC (TGC).

The Higher Level Trigger (HLT)

At the HLT, software-based trigger algorithms run for each signature. More precise measurement of p_{T} and position can be made at L2 with respect to L1 using fine calorimeter segments and precise muon chamber (MDT). Moreover, ID track information by the fast reconstruction are available at the HLT which improves the resolution of p_{T} by a combination with the muon chamber and calorimeters. Tighter p_{T} threshold at L2 is therefore applied and EF input rate is reduced to about 5 kHz. Well-reduced EF input rate allows the EF algorithm to access to the full detector information, which can perform offline-like, with high p_{T} resolution and high spacial resolution for each trigger signature. Required latencies at L2 and EF were 75 ms and 1 s, respectively, in 2012.

Typical Trigger Chains in 2012

The typical non-pre-scaled trigger chains in 2012 are namely `EF_e24vhi_medium1`, `EF_mu24i_tight` and `EF_xe80(T)_tclcw_loose`. They are trigger chains based on simple logic, targeting to collect events with single signature of high-p_{T} isolated electron, high-p_{T} isolated muon and high missing transverse energy, respectively. Trigger logics for each chain are explained in the followings.

- `EF_e24vhi_medium1`: At least one electron candidate with $p_{\mathrm{T}} > 18$ GeV at the L1 and $p_{\mathrm{T}} > 24$ GeV at the HLT is required. In addition, a relative track isolation requirement $\sum_{\Delta R<0.2} p_{\mathrm{T}}^{\mathrm{trk}}/E_{\mathrm{T}}^{e} < 0.1$ is required at EF,[8] and a small hadronic leakage is applied at L1.
- `EF_mu24i_tight`: At least one muon candidate with $p_{\mathrm{T}} > 15$ GeV at the L1 and $p_{\mathrm{T}} > 24$ GeV and $\sum_{\Delta R<0.2} p_{\mathrm{T}}^{\mathrm{trk}}/p_{\mathrm{T}}^{\mu} < 0.12$ at the EF is required. The isolation requirement rejects muons from heavy quark decays.
- `EF_xe80(T)_tclcw_loose`: Both `EF_xe80_tclcw_loose` and `EF_xe80T_tclcw_loose` require calorimeter-base $E_{\mathrm{T}}^{\mathrm{miss}}$ of > 40 GeV at L1, > 45 GeV at L2 and > 80 GeV at EF. `EF_xe80T_tclcw_loose` uses a complicated L1 algorithm, which does not take the first 3 bunch crossings in trains in order to cope with the out-of-time pileup contributions in the calorimeter pulse shape. `EF_xe80_tclcw_loose` was pre-scaled until May 2012. After May 2012, it was turned to be un-pre-scaled for the signal acceptance. The out-of-time pileup contributions are corrected or reduced by the other criteria (see Sects. 4.5.3 and 4.5.5).

In 2012, successful operation of the trigger and data acquisition system was achieved. The trigger efficiency of `EF_e24vhi_tight` to events containing a reconstructed isolated electron candidate with $p_{\mathrm{T}} > 24$ GeV is about 95 % at the barrel and 90 % at the endcap region [12]. The inefficiency of the electron trigger by 5–10 % occurrs at the HLT, while about 99–100 % efficiency is achieved at the L1. The efficiency of `EF_mu24i_tight` to events containing a reconstructed isolated muon with $p_{\mathrm{T}} > 24$ GeV is approximately 70 % at the barrel and 85 % at the endcap region [13]. The efficiency loss of the muon trigger is mainly caused by geometrical dead region of the L1 trigger chambers. The HLT efficiency with respect to L1 above the p_{T} threshold is about 98–99 %. The trigger efficiency of `EF_xe80_tclcw_loose` is about 100 % to events containing a jet with $p_{\mathrm{T}} > 60$ GeV and $E_{\mathrm{T}}^{\mathrm{miss}} > 150$ GeV. The large $E_{\mathrm{T}}^{\mathrm{miss}}$ of greater than 150 GeV and the soft muon (or electron) with $p_{\mathrm{T}} > 6\,(7)$ GeV are expected in the target stop signal. The trigger efficiency to low-p_{T} leptons is not sufficient, as discussed in Appendix G for muons. Therefore, `EF_xe80(T)_tclcw_loose` is used to collect the data in this analysis. Performance of `EF_xe80(T)_tclcw_loose` is discussed in detail in Sect. 3.1.2.

[8] $\sum_{\Delta R<0.2} p_{\mathrm{T}}^{\mathrm{trk}}$ is the sum of all track's p_{T} within a cone of $R = 0.2$ around the lepton.

Several combined-signature trigger chains are also prepared. For example:

- `EF_mu18_tight_mu8_EFFS` requires one muon with $p_{\mathrm{T}} > 18$ GeV passing all of L1, L2 and EF selection criteria and an additional muon with $p_{\mathrm{T}} > 8$ GeV at EF;
- `EF_e18vh_medium1_mu8` requires at least one electron with $p_{\mathrm{T}} > 18$ GeV passing L1, L2 and EF requirements and at least one muon with $p_{\mathrm{T}} > 8$ GeV passing L1, L2 and EF requirements.

These combined trigger chains will be more important in the LHC Run2, since higher event rate is expected.

References

1. L. Evans, P. Bryant, The LHC machine. JINST **3**, S08001 (2008)
2. ATLAS Collaboration. http://www.atlas.ch
3. F. Zimmermann, LHC: the machine. Lecture note in SLAC Summer Institute (2012). http://www-conf.slac.stanford.edu/ssi/2012/Presentations/Zimmermann.pdf
4. ATLAS Collaboration. https://twiki.cern.ch/twiki/bin/view/AtlasPublic/LuminosityPublicResults
5. M. Lamont, Status of the LHC. J. Phys. Conf. Ser. **455**, 012001 (2013)
6. ATLAS Collaboration, The ATLAS Experiment at the CERN Large Hadron Collider. JINST **3**, S08003 (2008)
7. ATLAS Collaboration, Alignment of the ATLAS Inner Detector and its Performance in 2012, ATLAS-CONF-2014-047. http://cds.cern.ch/record/1741021
8. ATLAS Collaboration. https://twiki.cern.ch/twiki/bin/view/AtlasPublic/TRTPublicResults
9. ATLAS Collaboration, Online Muon Reconstruction in the ATLAS Level-2 trigger system, ATL-DAQ-CONF-2005-013. http://cds.cern.ch/record/820782
10. K. Nagano, Algorithms, performance, and development of the ATLAS High-level Trigger, ATL-DAQ-PROC-2014-001. http://cds.cern.ch/record/1643488
11. K. Nagano, Algorithms, performance, and development of the ATLAS High-level Trigger, ATLAS-DAQ-SLIDE-2013-893. http://cds.cern.ch/record/1632445
12. ATLAS Collaboration. https://twiki.cern.ch/twiki/bin/view/AtlasPublic/EgammaTriggerPublicResults
13. ATLAS Collaboration, Performance of the ATLAS muon trigger in pp, collisions at $\sqrt{s} = 8$ TeV. arXiv:1408.3179

http://www.springer.com/978-981-10-0001-0

Search for Scalar Top Quarks and Higgsino-Like Neutralinos
SUSY Hunting With a "Soft" Lepton at the LHC
Nobe, T.
2016, XII, 224 p. 122 illus., 19 illus. in color., Hardcover
ISBN: 978-981-10-0001-0